Modelling and Control of Helical Microrobots

R.T.S. Kouwen

University of Twente, Faculty of Engineering Technology, Drienerlolaan 5, 7522 NB, Enschede, The Netherlands
r.t.s.kouwen@student.utwente.nl

ABSTRACT: Microrobotic surgery is a promising direction for non-invasive medical applications owing to their small size, and wireless actuation, and ability to access small spaces in a versatile manner. In this thesis, a motion control system for an untethered helical microrobot is investigated and designed. Resistive force theory was implemented to predict the swimming velocity of the helical robot. In addition, the method of regularized Stokeslets was applied to predict the fluid response and the flow field. A path following problem is formulated using a local Serret-Frenet frame. Chained form is used to address the kinematics of the robot, as to decouple the inputs and outputs of the controller. The results from the resistance force-based model provide a linear relation between linear and rotational velocity and the required magnetic torques for a range of operating velocities.

Key words: helical robot, magnetic, RFT, closed-loop control, medical, rotating dipole

1 INTRODUCTION

Helical microrobots have potential biomedical applications in the field of targeted therapy and biomedicine. It is important to develop a numerical model to predict the swimming speed of microrobots to enable them to swim in conditions similar to those encountered in vivo. Both the challenges of high flow rates of bodily fluids and localization of the microrobot in the body must be addressed in order to translate these microdevices into in vivo applications.

For actuating the microrobot, a single rotating permanent magnet configuration has been investigated by Fountain *et al.* [1]. Mahoney *et al.* presented additions in orientation control [2] and the management of the undesirable magnetic force [3]. The approach presented by Hosney *et al.* uses two synchronized permanent magnets which cancel the magnetic force along the lateral direction of the helical robot and produce pure torque. [4]. Controlling the microrobot over different trajectories has been achieved in open-loop by Ghost and Fischer [5, 6] and closed-loop by Xu *et al.* [7]. Recently, aspects such as the influence of the capillary wall [8, 9] and time varying flow rate [10, 11] have also been investigated. Another challenge, working with ultrasound, MRI and X-ray feedback with microrobots has been proposed by Nelson *et al.* [12]. Ultrasound was applied by Khalil *et al.* [13], MRI by Martel *et al.* [14] and X-ray detection by Nguyen *et al.* [15]. Still, detection is a challenge when scaling microrobots down, geometry needs to be investigated for both detection and swimming performance.

The focus of this thesis is a motion control model for the microrobot, which allows for the evaluation of geometry. We investigate the physical model of the microrobot through resistive force theory (RFT) and look at required magnetic torque. Additionally the constraints on the kinematics of the microrobot are put into chained form and are applied to a path following formulation.

2 MODELLING OF HELICAL MICROROBOTS

The focus lies on the modelling and computations that are required for evaluating geometry. The dynamic system is modelled with RFT [16] and consequently using the method of regularized Stokeslets [17]. After this the kinematics are treated and the control formulation is stated.

2.1 Modelling: magnetic actuation

The microrobot, shown in Figure 1, is parameterized as a rigid helix. A magnetic material is attached to one of its ends, also referred to as the head.

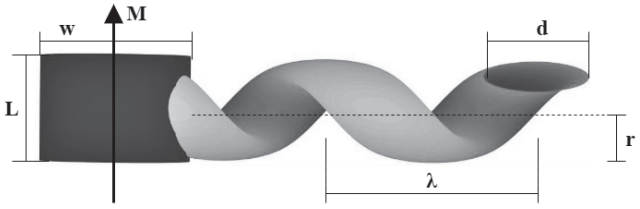

Figure 1: Helical microrobot geometry. L is the length of the head, w is the diameter of the head, λ is the wavelength of the helix, r the radius of the helix and d is the thickness.

For the magnetic head, we assume a cylindrical permanent magnet with a constant magnetization ($\mathbf{M}$). Under influence of a rotating external magnetic field, the microrobot will try to align the magnetization of the magnetic head with the external magnetic field. As the external magnetic field is rotated around the axis of helix, the microrobot will correspondingly rotate along its axis and consequently translate. The external magnetic field is assumed uniform, therefore the gradient of the field is zero. From this follows that the magnetic force is zero. Only magnetic torque is generated [18].

$$\mathbf{T_m} = \mathbf{M} \times \mathbf{B} \tag{1}$$

In equation (1), $\mathbf{T_m}$ is the magnetic torque. Further, $\mathbf{M}$ and $\mathbf{B}$ are the magnetic moment of the microrobot and the external magnetic field.

2.2 Modelling: drag-based thrust

The robot swims in a low *Re*-number medium, where viscous forces dominate. This approach allows the Navier-Stokes equations to be simplified to the Stokes equations, from which the drag force and torque on the microrobot can be modelled. At millimeter scale it has been shown that these equations still provide an acceptable approximation even though the weight of the robot influences the motion [12]. On the other hand, Nelson *et al.* have indicated that gravity effects become more significant with the weight [12]. The gravitational force and torque are obtained from Khalil *et al.* [19].

$$\begin{bmatrix} \mathbf{F_g} \\ \mathbf{T_g} \end{bmatrix} = \begin{bmatrix} V(\rho_r - \rho_f)\mathbf{R}_{\mathbf{O}}^{\mathbf{B}}\,{}^{\mathbf{O}}\mathbf{g} \\ (\mathbf{r_{cov}} - \mathbf{r_{com}}) \times \mathbf{F_g} \end{bmatrix} \tag{2}$$

Here V is the volume of the robot, ρ_r and ρ_f the density of the robot and medium. Further, $\mathbf{R}_{\mathbf{O}}^{\mathbf{B}}$ is the rotation matrix from a stationary frame to the robot frame and ${}^{\mathbf{O}}\mathbf{g}$ is the gravity in the stationary frame. Furthermore, $\mathbf{r_{cov}} - \mathbf{r_{com}}$ is the difference between the center of volume and mass of the robot.

The equation of motion is represented by drag, gravity and magnetic components. Inertia does not appear as it is negligible in the Stokes equations. We consider far field fluid flow and therefore assume no effect of boundaries on the fluid flow, which completes the model.

$$\begin{bmatrix} \Sigma\mathbf{F} \\ \Sigma\mathbf{M} \end{bmatrix} = \begin{bmatrix} \mathbf{F_d} + \mathbf{F_g} + \mathbf{F_m} \\ \mathbf{T_d} + \mathbf{T_g} + \mathbf{T_m} \end{bmatrix} = \begin{bmatrix} 0 \\ 0 \end{bmatrix} \tag{3}$$

In equation (3), $\mathbf{F_d}$ is the drag force, $\mathbf{F_m}$ the magnetic propulsive force and $\mathbf{T_d}$ is the drag torque.

2.3 Modelling: resistive force theory

In order to model the drag on the helix of the microrobot, RFT provides a useful method to solving equation (4). Drag force and torque are assumed linearly dependent on velocity for the flagellum [16]. The appropriate force and torque can be found by integrating over the helix. From Chwang and Wu the integration constants are available [20].

An important and limiting assumption in this method is that the helix is rigid and thin. The drag force from the rotation of the thin flagellum about its own center is neglected. This allows the drag torque to be expressed as the cross product of drag force and a moment arm related to the position of evaluation.

$$\begin{bmatrix} \mathbf{F_d} \\ \mathbf{T_d} \end{bmatrix} = \begin{bmatrix} \mathbf{A} & \mathbf{B} \\ \mathbf{B^T} & \mathbf{C} \end{bmatrix} \begin{bmatrix} \mathbf{V} \\ \mathbf{\Omega} \end{bmatrix} \tag{4}$$

In addition to the drag from the flagellum, the drag from the permanent magnet also need to be modelled, as it contributes to the drag force. Superposition is used as the Stokes equations are linear and reversible, so the contribution of the head is summed with that of the helix.

From this model we can evaluate the geometrical properties. As we are interested in the linear and rotational velocity, we can now use equation (3) and (4) to derive them from the magnetic torque.

2.4 Modelling: method of regularized Stokeslets

The method of regularized Stokeslets allows us to expand the applications of the model. Flexible geometry is allowed, although not applied in this case. In addition, evaluation over surfaces is possible, which allows any shape instead of only thin filament shapes from RFT. The method of regularized Stokeslets allows for evaluation of the resulting flow velocity in the medium as well [17, 21]. Moreover, it allows for heterogeneous properties, such as blood cells. Bruce

provides a simulation package in Matlab to apply the method [22].

2.5 Kinematics of the helical robot

The microrobot has to follow a path in the medium. The actuation is untethered, Figure 2 shows the kinematics of the situation.

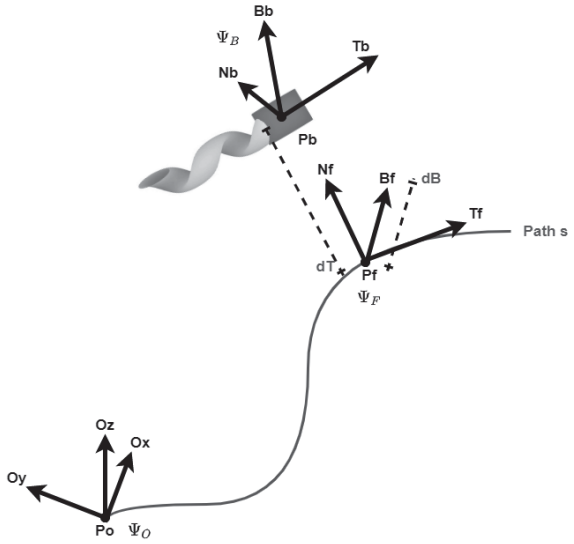

Figure 2: Kinematics and frames of the microrobot and path

The following orthonormal frames and parameters are defined for Figure 2.

- Ψ_B, the body frame of the microrobot, centered at the center of mass. The tangent vector $\mathbf{T_b}$ is normal to the magnetisation of the head.
- Ψ_F, the Serret-Frenet frame on the path defined by parametrization *s*.
- Ψ_O, the stationary origin frame. The origin is located at the beginning of path *s*.

We can transform from each frame with the transformation matrices defined below.

- $\mathbf{H_B^O}$, this equals rotation along the O_{xyz} axiis to $[\mathbf{T_b}\ \mathbf{N_b}\ \mathbf{B_b}]$ and the translation of the origin defined by the vector spanned between $\mathbf{P_O}$ and $\mathbf{P_b}$.
- $\mathbf{H_F^O}$, this equals the rotations along the O_{xyz} axiis and the translation of the origin to the Serret-Frennet frame.

The path should be a smooth curve in 3D space. From the path $\mathbf{r}$, constructed in frame Ψ_O, the parameters τ and c follow from the Frenet-Serret formulas.

$$\tau = \frac{|\dot{\mathbf{r}} \times \ddot{\mathbf{r}}|}{|\dot{\mathbf{r}}|^3} \tag{5}$$

$$c = \frac{|\dot{\mathbf{r}} \times \ddot{\mathbf{r}}|\dddot{\mathbf{r}}}{|\dot{\mathbf{r}} \times \ddot{\mathbf{r}}|^2} \tag{6}$$

In equation (5), τ is the torsion and in (6) c is the curvature.

2.6 Physical model

The physical plant follows from the torque and force balance in section 2.3. In equation (4) the drag force and torque are mentioned. The derivation follows from integrating the drag force and torque contributions from each segment over the complete helix. In addition, these contributions are projected from a local segment frame Ψ_s, a Serret-Frenet frame, to the frame Ψ_B fixed to the microrobot.

The derivation for $\mathbf{F_d}$ and $\mathbf{T_d}$ follow below. Equation (7) expresses the drag force proportional to velocity, this assumption follows from RFT [23].

$$^{\mathbf{s}}\mathbf{dF_d} = \mathbf{C}\ ^{\mathbf{s}}\mathbf{V_s} = \mathbf{C}\ (\mathbf{R_s^B})^T\ ^{\mathbf{B}}\mathbf{V_s} \tag{7}$$

In equation (7), $^{\mathbf{s}}\mathbf{dF}$ is the force locally on a helix segment and $^{\mathbf{s}}\mathbf{V_s}$ the speed of the segment in the travelling Serret-Frenet frame Ψ_s. We transform to the Ψ_B frame with the rotation matrix $\mathbf{R_s^B}$.

$$\mathbf{R_s^B} = [\hat{\mathbf{T}}\ \hat{\mathbf{N}}\ \hat{\mathbf{B}}] \tag{8}$$

Where $\hat{\mathbf{T}}$, $\hat{\mathbf{N}}$ and $\hat{\mathbf{B}}$ are defined by the Serret-Frenet equations.

$$\hat{\mathbf{T}} = \frac{\mathbf{r}'}{|\mathbf{r}'|} = \tag{9}$$

$$\hat{\mathbf{N}} = \frac{1}{c}\frac{d\hat{\mathbf{T}}}{ds} \tag{10}$$

$$\hat{\mathbf{B}} = \hat{\mathbf{T}} \times \hat{\mathbf{N}} \tag{11}$$

Here c follows from equation (6) and $\mathbf{r}$ is the helix parametrization.

$$\mathbf{r} = \left[\tfrac{W}{2}\cos(s) \quad \tfrac{W}{2}\sin(s) \quad \tfrac{L}{2N\pi}s\right] \tag{12}$$

Consequently we can now define rotation matrix $\mathbf{R}_{\mathbf{s}}^{\mathbf{B}}$ from equation (8).

$$\mathbf{R}_{\mathbf{s}}^{\mathbf{B}} = \begin{bmatrix} \frac{-a}{2\sqrt{a^2+b^2}}\sin(s) & \frac{-a}{2\sqrt{a^2+b^2}}\cos(s) & b \\ -\cos(s) & -\sin(s) & 0 \\ \frac{b}{\sqrt{a^2+b^2}}\sin(s) & \frac{b}{\sqrt{a^2+b^2}}\cos(s) & \frac{a}{\sqrt{a^2+b^2}} \end{bmatrix} \tag{13}$$

Where in equation (13), $a = \frac{W}{2}$ and $b = \frac{L}{2N\pi}$. Furthermore, ${}^{\mathbf{B}}\mathbf{V}_{\mathbf{s}}$, the linear velocity of the segment is expressed in the linear and rotational velocity of the body.

$${}^{\mathbf{B}}\mathbf{V}_{\mathbf{s}} = {}^{\mathbf{B}}\mathbf{V} + {}^{\mathbf{B}}\boldsymbol{\Omega} \times \mathbf{p} \tag{14}$$

Where ${}^{\mathbf{B}}\mathbf{V}$ is the linear velocity on the body in the Ψ_B frame and $\mathbf{p} = \mathbf{r}(s)$ the distance between the origin of Ψ_B and the local point on the helix. Next we substitute equation (13) and (14) in equation (7).

$$\mathbf{R}_{\mathbf{s}}^{\mathbf{B}}\ {}^{\mathbf{s}}\mathbf{dF_d} = \mathbf{R}_{\mathbf{s}}^{\mathbf{B}}\ \mathbf{C}\ (\mathbf{R}_{\mathbf{s}}^{\mathbf{B}})^T\ ({}^{\mathbf{B}}\mathbf{V} + {}^{\mathbf{B}}\boldsymbol{\Omega} \times \mathbf{p}) \tag{15}$$

Further, equation (15) can be expressed as ${}^{\mathbf{s}}\mathbf{dF_d}$.

$$\begin{aligned} {}^{\mathbf{B}}\mathbf{dF_d} = {} & [\mathbf{R}_{\mathbf{s}}^{\mathbf{B}}\ \mathbf{C}\ (\mathbf{R}_{\mathbf{s}}^{\mathbf{B}})^T]\ {}^{\mathbf{B}}\mathbf{V} + \\ & [\mathbf{R}_{\mathbf{s}}^{\mathbf{B}}\ \mathbf{C}\ (\mathbf{R}_{\mathbf{s}}^{\mathbf{B}})^T\ Sk[-\mathbf{p}]\ ]\ {}^{\mathbf{B}}\boldsymbol{\Omega} \end{aligned} \tag{16}$$

Here Sk is the skew-symmetric operator. Equation (16) relates to $\mathbf{A}$ and $\mathbf{B}$ matrices from equation (4), the $\mathbf{C}$ matrix is defined below.

$$\mathbf{C} = \begin{bmatrix} C_s & 0 & 0 \\ 0 & C_n & 0 \\ 0 & 0 & C_n \end{bmatrix} \tag{17}$$

From equation (17), C_n and C_s are the drag constants from Chwang and Wu [20].

$$C_s = \frac{2\pi\mu}{\ln(0.72\frac{L}{N}\pi/W) + 0.5} \tag{18}$$

$$C_n = \frac{4\pi\mu}{\ln(0.72\frac{L}{N}\pi/W) - 0.5} \tag{19}$$

In equations (18) and (19), μ is the viscosity. C_s and C_n were derived from a 2-d sinusoidal shaped flagellum. However, the constants are also applicable to general 3-d flagella, as the constant C_n is applicable to both *B* and *N* directions.

Next is the derivation for $\mathbf{T_d}$, for which we can use a similar assumption relating torque and rotational velocity [20].

$${}^{\mathbf{s}}\mathbf{dT_d} = C_m\boldsymbol{\Omega} \tag{20}$$

Alternatively, we can also use the definition of torque as the cross product of the moment arm, $\mathbf{p}$ and the force ${}^{\mathbf{B}}\mathbf{dF_d}$.

$${}^{\mathbf{B}}\mathbf{dT_d} = Sk[\mathbf{p}]\ {}^{\mathbf{B}}\mathbf{dF_d} \tag{21}$$

Using the alternative, equation (21) can be simplified by using matrix manipulations and the definition of the skew symmetric matrix, $Sk[-\mathbf{p}] = Sk[\mathbf{p}^T]$.

$${}^{\mathbf{B}}\mathbf{dT_d} = Sk[\mathbf{p}][\mathbf{R}_{\mathbf{s}}^{\mathbf{B}}\ \mathbf{C}\ (\mathbf{R}_{\mathbf{s}}^{\mathbf{B}})^T]\ {}^{\mathbf{B}}\mathbf{V} + \mathbf{C}\ {}^{\mathbf{B}}\boldsymbol{\Omega} \tag{22}$$

Note from equation (22) that the matrix before ${}^{\mathbf{B}}\mathbf{V}$, can be written as $\mathbf{B^T}$ after applying the matrix rules for transposition. So this agrees with the model from equation (4). Additionally, $\mathbf{C}$ in equation (4) is also visible to indeed be $\mathbf{C}$ in equation (22).

What is left is to integrate ${}^{\mathbf{B}}\mathbf{dF_d}$ and ${}^{\mathbf{B}}\mathbf{dT_d}$ over the helix, which results in the drag force and torque over the helix. Moreover, the drag force and torque of the magnetic head are included by superposing it with the drag force and torque for the helix. This is an operation depending upon the geometry and fluid properties used.

2.7 Control formulation

The system is non-holonomic, the total linear velocity was taken out of the control and considered an input. The resulting system will be derived in this section, but the consequence of considering velocity as an input is that the system is linear time invariant. Therefore, state feedback is used for control.

Path following is chosen over trajectory tracking. The error performance in space is more important than that in time, therefore path following is preferred [7]. The reference signal is constructed by translating the path following formulation to a trajectory tracking signal. This transformation has negative effects, as we now have the limitations from trajectory tracking in the L_2 norm error [24].

The reference signal is constructed subsequently.

$${}^{\mathbf{O}}\mathbf{r}(t) = {}^{\mathbf{O}}\mathbf{r_0} + {}^{\mathbf{O}}\mathbf{v_F}t \tag{23}$$

Here ${}^{\mathbf{O}}\mathbf{r}(\mathbf{t})$ is the reference position in time, ${}^{\mathbf{O}}\mathbf{r_0}$ is the initial position. Further, the constant velocity of the microrobot in tangent direction is transformed to the Frenet frame. The transformation is in equation (24) and (25), here the $\mathbf{N_f}$ and $\mathbf{B_f}$ directions are zero, such that the velocity is bounded by the path $\mathbf{r}$. This ensures the distance between the microrobot and $\mathbf{r}(t)$ is zero along the tangent direction in the Frenet frame.

$$ {}^{\mathbf{O}}\mathbf{v_F} = \mathbf{H_F^O}\ \mathbf{H_O^{*F}}\ \mathbf{H_B^O}\ {}^{\mathbf{B}}\mathbf{v_b} \tag{24} $$

In equation (25) the rotation matrices are defined, the vectors **T, N** and **B** are according to the standard Serret-Frenet formulas.

$$ {}^{\mathbf{O}}\mathbf{v_F} = [\mathbf{T_F}\ \mathbf{N_F}\ \mathbf{B_F}]\ [\mathbf{T_F}\ \mathbf{0}\ \mathbf{0}]^{-1}\ [{}^{\mathbf{O}}\mathbf{T_B}\ \mathbf{0}\ \mathbf{0}]\ {}^{\mathbf{O}}\mathbf{v_b} \tag{25} $$

Because $\mathbf{v_b}$ is only non-zero in the tangent direction for the microrobot in Ψ_B, $\mathbf{H_B^O}$ is defined in this direction as ${}^{\mathbf{O}}\mathbf{T_B}$.

$$ {}^{\mathbf{O}}\mathbf{T_B} = [\cos\theta_{ib}\cos\theta_{db},\ \ -\cos\theta_{ib}\sin\theta_{db},\ \ \sin\theta_{ib}]^T \tag{26} $$

Here θ_{ib} is the inclination angle of the body and θ_{db} the direction angle of the body, both according to Figure 3.

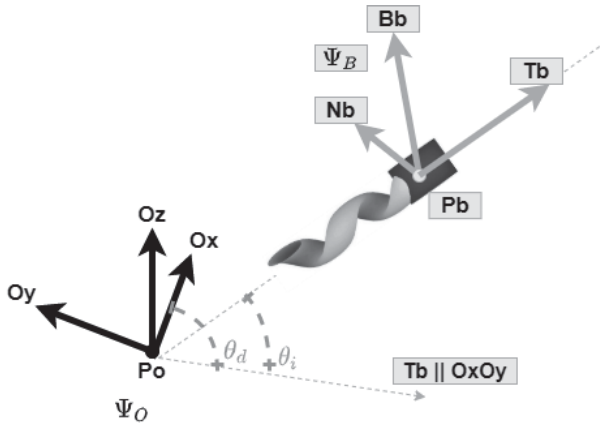

Figure 3: Error in angle of the microrobot

The inputs to the system are $({}^B\Omega_y, {}^B\Omega_z)$, which are the rotations over the body axiis of the microrobot.

The state vector is $(d_y,\ d_z,\ \theta_{ie},\ \theta_{de})$. As the problem is a path following formulation, the distance in $\mathbf{T_F}$ is zero and thus not included in the state vector. In the state vector, d_y and d_z are the distances in the $\mathbf{N_F}$ and $\mathbf{B_F}$ axiis between the microrobot and the reference point on the path.

$$ \begin{bmatrix} 0 \\ N \\ B \end{bmatrix} = \begin{bmatrix} 0 \\ d_y \\ d_z \end{bmatrix} = {}^{\mathbf{F}}\mathbf{P_b} = \mathbf{H_O^F}\ {}^{\mathbf{O}}\mathbf{P_b} \tag{27} $$

Here $\mathbf{P_b}$ is the position of the body of the microrobot.

$$ {}^{\mathbf{O}}\mathbf{P_b} = {}^{\mathbf{O}}\mathbf{P_{b0}} + {}^{\mathbf{O}}\mathbf{v_b}\ t \tag{28} $$

Here ${}^{\mathbf{O}}\mathbf{P_{b0}}$ is the initial postion of the body.

The angles θ_{ie} and θ_{de} are the difference between the inclination (θ_i) and direction (θ_d) angle of the path and the microrobot tangent.

$$ \theta_i = \theta_i + \Omega_y\ dt = \int_t^{t_0} \Omega_y\ dt \tag{29} $$

$$ \theta_d = \theta_d + \Omega_z\ dt = \int_t^{t_0} \Omega_z\ dt \tag{30} $$

$$ \theta_{ie} = \theta_{ib} - \theta_{ir} \tag{31} $$

$$ \theta_{de} = \theta_{db} - \theta_{dr} \tag{32} $$

In equation (31), θ_{ib} is the inclination angle of the body and θ_{ir} that of the path. Also, in equation (32) θ_{db} is the direction angle of the body and θ_{dr} that of the path.

3 RESULTS

3.1 Control implementation of chained form

Samson offers an analysis and application of the chained formulation for path following for non holonomic mobile robots [25]. In addition, the notion was presented that the non-linear chained form equations become linear when the first input is taken out outside of the control. In case of helical microrobots the velocity v_b is taken at a constant value, resulting in a system that is also time invariant. Oulmas *et al.* applies this and provides the chained form as in equations (33) and (34) [26, 27].

$$ {}^{O}\Omega_z = (u_2 - \gamma_{22})\gamma_{21}^{-1}) \tag{33} $$

$$ {}^{O}\Omega_y = (u_3 - \gamma_{33} - \gamma_{32}\gamma_{21}^{-1}(u_2 - \gamma_{22}))\gamma_{31}^{-1} \tag{34} $$

Here γ_{21} till γ_{33} are functions of the path $\mathbf{r}$, s, τ, the input ${}^{B}v_t$ and the error d_y, d_z, θ_{ie}, θ_{de}.
u_1-u_3 and x_1-x_5 are presented in equations (35)-(42) [26].

$$u_1 = {}^{B}v_T \cos\theta_{de} \cos\theta_{ie}(1 - cd_y)^{-1} \tag{35}$$
$$u_2 = -k_{d1}u_1x_2 - k_{t1}|u_1|x_3 \tag{36}$$
$$u_3 = -k_{d2}u_1x_4 - k_{t2}|u_1|x_5 \tag{37}$$
$$x_1 = s \tag{38}$$
$$x_2 = d_y \tag{39}$$
$$x_3 = (1 - cd_y)\tan\theta_{de} + \tau d_z \tag{40}$$
$$x_4 = d_z \tag{41}$$
$$x_5 = \tan\theta_{ie}(cd_y - 1)(\cos\theta_{de})^{-1} - \tau d_y \tag{42}$$

Here k_{t1}, k_{t2}, k_{d1} and k_{d2} are the proportional and derivative control parameters.

3.2 Control physical plant

In this section the state space equations of the physical model are presented. Using the results from sections 2.1 and 2.6 the equilibria can be expressed.

$$\Sigma\, {}^{\mathbf{B}}\mathbf{F} = \mathbf{A}\, {}^{\mathbf{B}}\mathbf{V} + \mathbf{B}\, {}^{\mathbf{B}}\boldsymbol{\Omega} + {}^{\mathbf{B}}\mathbf{F_g} = 0 \tag{43}$$
$$\Sigma\, {}^{\mathbf{B}}\mathbf{T} = \mathbf{B^T}\, {}^{\mathbf{B}}\mathbf{V} + \mathbf{C}\, {}^{\mathbf{B}}\boldsymbol{\Omega} + {}^{\mathbf{B}}\mathbf{T_g} + \mathbf{M} \times \mathbf{B} = 0 \tag{44}$$

Equation (43) can be rewritten in terms of linear velocity.

$${}^{\mathbf{B}}\mathbf{V} = \mathbf{A}^{-1}(-{}^{\mathbf{B}}\mathbf{F_g} - \mathbf{B}\, {}^{\mathbf{B}}\boldsymbol{\Omega}) \tag{45}$$

Alternatively, equation (43) can be rewritten in terms of rotational velocity.

$${}^{\mathbf{B}}\boldsymbol{\Omega} = \mathbf{B^{-1}}(-{}^{\mathbf{B}}\mathbf{F_G} - \mathbf{A}\, {}^{\mathbf{B}}\mathbf{V}) \tag{46}$$

Substituting equation (43) in (44) provides the system expressed in rotational velocity.

$$\begin{aligned} &{}^{\mathbf{B}}\boldsymbol{\Omega} - (\mathbf{B}^T\mathbf{A}^{-1}\mathbf{B} - \mathbf{C})^{-1}\, \mathbf{M} \times \mathbf{B} = \\ &(\mathbf{B}^T\mathbf{A}^{-1}\mathbf{B} - \mathbf{C})^{-1}({}^{\mathbf{B}}\mathbf{T_g} - \mathbf{B^T}\mathbf{A^{-1}}\, {}^{\mathbf{B}}\mathbf{F_g}) \end{aligned} \tag{47}$$

Or alternatively for the system expressed in linear velocity, we substitute equation (45) in (44).

$$\begin{aligned} &{}^{\mathbf{B}}\mathbf{V} + (\mathbf{B^T} - \mathbf{CB^{-1}A})^{-1}\, \mathbf{M} \times \mathbf{B} = \\ &(\mathbf{B^T} - \mathbf{CB^{-1}A})^{-1}\, (\mathbf{CB^{-1}F_g} - \mathbf{T_g}) \end{aligned} \tag{48}$$

Given that we use the chained form from section 3.1 and only require $\boldsymbol{\Omega}$, then equation (47) is used to derive the differential equation and state space representation. Gravity is excluded from the state space equation, as the transformation matrix $\mathbf{R_O^B}$ from equation (2) can not be defined from the kinematics from section 3.1.

The system input $\mathbf{M} \times \mathbf{B}$ is considered as a proportional constant multiplied with error, the equation (46) can be rewritten as an ordinary differential equation. The error is defined as $\mathbf{e} = \theta_\mathbf{f} - \theta_\mathbf{b}$, where $\theta_\mathbf{f}$ are the reference angles and $\theta_\mathbf{b}$ the body angles.

$$\begin{aligned} &\dot{\theta_\mathbf{b}} + k[\ [\mathbf{B}^T\mathbf{A}^{-1}\mathbf{B}] - [\mathbf{C}]\ ]^{-1}\, \theta_\mathbf{b} = \\ &\qquad k[\ [\mathbf{B}^T\mathbf{A}^{-1}\mathbf{B}] - [\mathbf{C}]\ ]^{-1}\, \theta_\mathbf{f} + \\ &(\mathbf{B}^T\mathbf{A}^{-1}\mathbf{B} - \mathbf{C})^{-1}({}^{\mathbf{B}}\mathbf{T_g} - \mathbf{B^T}\mathbf{A^{-1}}\, {}^{\mathbf{B}}\mathbf{F_g}) \end{aligned} \tag{49}$$

Equation (49) can be converted to the state space representation.

$$\begin{aligned} \dot{\theta_\mathbf{b}} = &-k[\ [\mathbf{B}^T\mathbf{A}^{-1}\mathbf{B}] - [\mathbf{C}]\ ]^{-1}\, \theta_\mathbf{b} + \\ &k[\ [\mathbf{B}^T\mathbf{A}^{-1}\mathbf{B}] - [\mathbf{C}]\ ]^{-1}\, \theta_\mathbf{f} \end{aligned} \tag{50}$$
$$\mathbf{y} = [\mathbf{I}]\ \theta_\mathbf{b} + 0\ \theta_\mathbf{f} \tag{51}$$

Equations (50) and (51) were derived in controllable canonical form, because we only considered θ. If we were to not use the chained equations, the error would both be in angle and position. In that case we need to introduce a different set of governing kinematic equations for the non-holonomic robot and solve the state space representation in observable canonical form instead.

3.3 Rotational and linear velocity

Using the results from section 3.2, equation (45) was used to provide the linear velocity against rotational speed. The values used for the $\mathbf{A}$, $\mathbf{B}$ and $\mathbf{C}$ matrices are provided by Mahoney *et al.* [6], but they can also be derived from section 2.6.

The geometric properties used during the simulations are displayed in Table 3.3.

Table 1: Properties used in regularized stokeslets modelling. The geometric properties are according to Figure 1.

Helix	
λ *(m)*	6 10^{-4}
d (m)	1.2 10^{-4}
r (m)	2.5 10^{-4}
N	2
Medium	Homogenous
viscosity (Pa s)	1 (glycerin)
Magnet	
Shape	Cylindrical
L (m)	5 10^{-4}
w (m)	1.5 10^{-4}

The linear velocity is projected against rotational velocity from these properties. The relation is linear up to the step out frequency. The step out frequency is not listed, as this depends on the magnitude of the magnetic field and the magnetisation of the microrobot. We do not assume a value for these. In Figure 4 the velocity relation is displayed.

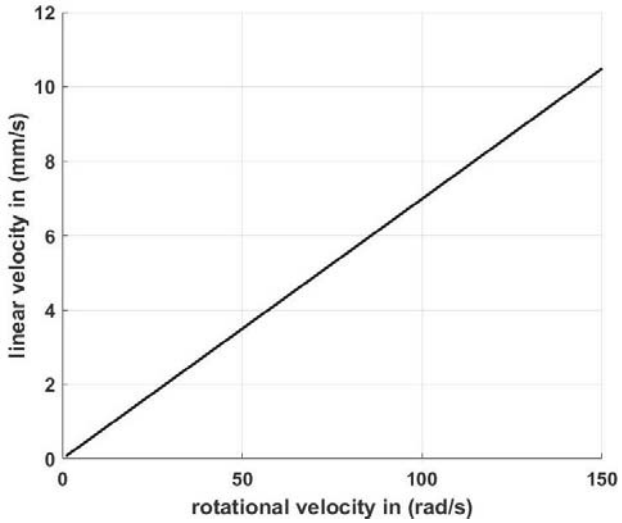

Figure 4: Relation between rotational and linear velocity

3.4 Chained formulation

The chained form equations from section 3.1 were implemented in a Simulink model. First off, the path following formulation is demonstrated in Figure 5. An arbitrary signal for the microrobot position is used, in order to show how the reference follows. The reference trajectory keeps the error in position minimal and does not increase the error by continuously progressing as trajectory tracking would.

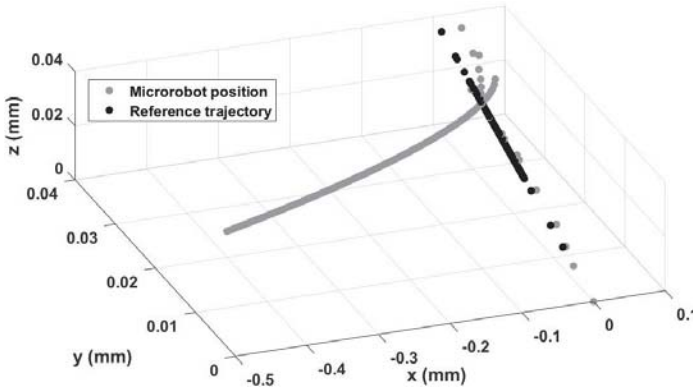

Figure 5: Path following reference signal demonstration

Further, in Figure 6 the error in path following is demonstrated. The performance is not as expected, it is visible that initially the controller follows the curve, but overcorrects the curvature and does not return to the reference. The reasons for this are reserved for the discussion in Section 4.

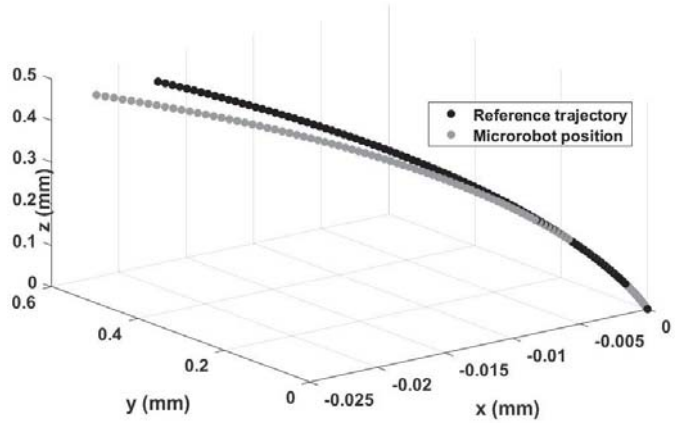

Figure 6: Path following of the microrobot

3.5 Physical model

The physical model from Section 3.2 was implemented in a Matlab script, from which the required magnetic torque can be calculated. Figure 7 shows the relation between the phase difference in M and B for a set of fixed values, only varying phase difference.

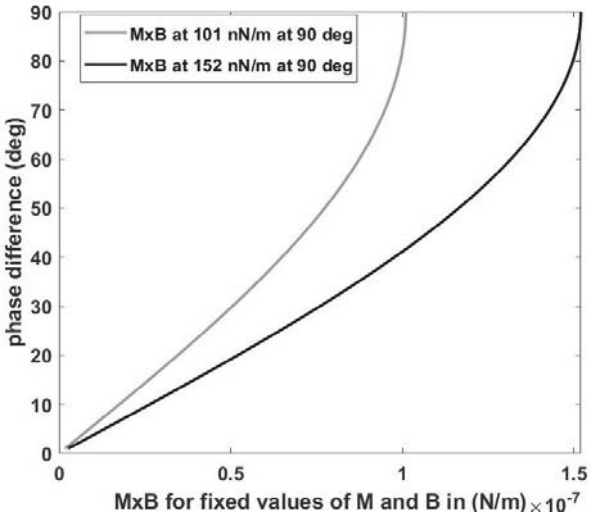

Figure 7: Fixed values of M and B vs phase difference

Further, the step out frequency or rotational speed is reached at 90 degree phase difference, where the cross product is at maximum. Figure 8 shows the relation between rotational speed and required torque at 90 degrees phase difference.

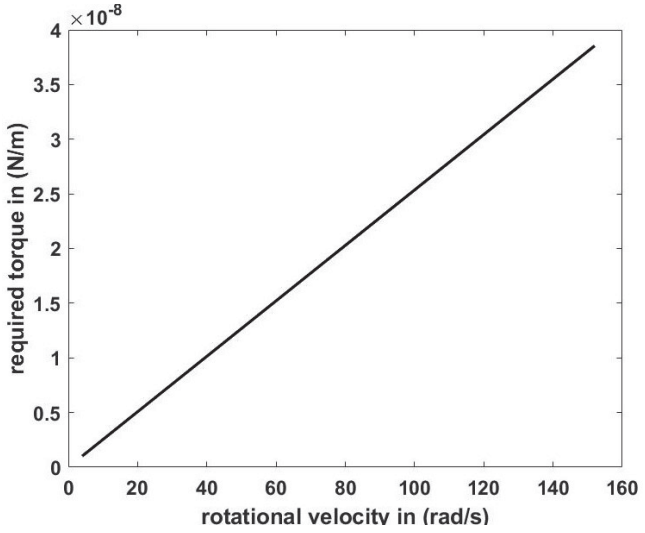

Figure 8: Rotational velocity vs required magnetic torque at 90 deg phase difference

The torque in Figure 8 was applied along the directional axis of the microrobot, which resulted in the rotational velocity of the same axis.

4 DISCUSSION

In section 3.2 gravity was excluded from the state space equation, as the transformation matrix $\mathbf{R}_{\mathrm{O}}^{\mathrm{B}}$ from equation (2) could not be defined from the kinematics from section 3.1. In the chained form, the inclination and direction angles are only constructed. This is sufficient to define the tangent in the stationary frame, yet this is not sufficient to define the normal and binormal axiis, which are required for $\mathbf{R}_{\mathrm{O}}^{\mathrm{B}}$. If we still want to account for gravity, modelling it as a disturbance is a possibility. Otherwise different kinematics are required that do allow for the complete $\mathbf{R}_{\mathrm{O}}^{\mathrm{B}}$ matrix.

In Section 3.3 the relation between speed and rotational velocity was investigated. A limitation here is that the simulation used for Figure 4 assumed a spherical magnetic head. In our case, we intend to simulate a cylindrical head. However, the relations for Stokes flow allow for superposition and the Stokes drag force from the head is linearly dependent on velocity. Therefore, the impact is that the inclination of the slope from the linear relation will only change.

In section 3.4 the results from the controller built of the chained formulation presented by Oulmas *et al.* [27] were not as expected. Without any physical model behind it, it is surprising the error behaves as it does in Figure 6. Despite varying the control coefficients the model eventually deviates from the reference. It was checked that the path following reference signal does not malfunction and this did not influence the results. However, upon logging the signals it appears that γ_{21} till γ_{33} influence Ω_{xy} significantly. Also, because the γ terms multiply with the controls u_2 and u_3, they directly influence the magnitude of the control.

It is important to note that this formulation requires the microrobot to be close to reference, which is why in literature often the robot is initially guided to the reference trajectory. In our simulations we accounted for this, but it did not improve the results sufficiently. In future work it would be suggested to start over with a simpler model than that of Oulmas *et al.* and to allow for continuous time operation.

In Section 3.4, the required magnetic torque was evaluated using the physical model derived in Section 3.2. Comparing the results to research, the result in Figure 8 is linear as expected [1, 12]. In addition, we compared the results in torque magnitude from Figure 8 to the results of Khalil *et al.* [13], which uses a setup with a magnetisation and magnetic field that

is capable of a maximum torque of $9.510^{-7}Nm^{-1}$. For a step out rotational velocity of 150 rad/s, our model, with the geometry of [13], requires a torque of $1.510^{-7}Nm^{-1}$. This is not unreasonable as the model from Khalil *et al.* experiences more drag, as that microrobot also rubs against blood clots to remove them.

5 CONCLUSION

In this thesis resistive force theory was used to simulate the drag force and torque on a helical microrobot that swims in a viscous medium. The model is reserved to thin structures. A path following problem is formulated for a reference that satisfies the Serret-Frenet constraints. The problem is addressed with a control formulation using the chained formulation, however the behaviour was not as expected. The results from dynamic model that simulates the physical plants were as expected and were verified with the results from other sources. The current model allows for the evaluation of velocity performance for various geometric parameters. For future work, it would be interesting to investigate the open-loop motion response. Further, expanding the dynamic model by combining the resistive force derived dynamics with the kinematic relations in chained form would be a future challenge.

REFERENCES

1. T.W.R. Fountain, P.V. Kailat, and J.J. Abbott, "Wireless control of magnetic helical microrobots using a rotating-permanent-magnet manipulator", In: *Proc.* , *IEEE ICRA*, (2010), pp. 576–581.

2. A.W. Mahoney, D.L. Cowan, K.M. Miller, and J.J. Abbott, "Control of untethered magnetically actuated tools using a rotating permanent magnet in any position", In: *Proc.* , *IEEE ICRA*, (2012), pp. 3375–3380.

3. A.W. Mahoney, S.E. Wright, and J.J. Abbott, "Managing the attractive magnetic force between an untethered magnetically actuated tool and a rotating permanent magnet", In: *Proc.* , *IEEE ICRA*, (2013), pp. 5366–5371.

4. A. Hosney, A. Klingner, S. Misra, and I.S.M. Khalil, "Propulsion and steering of helical magnetic microrobots using two synchronized rotating dipole fields in three-dimensional space", In: *Proc. , IEEE IROS,* W. Burgard, Sept. 2015, pp. 1988-1993.

5. A. Ghost and P. Fischer, "Controlled propulsion of artificial magnetic nanostructured propellers", *Nano Lett.*, Jun. 2009, vol. 9, no. 6, pp. 2243-2245.

6. A.W. Mahoney, J.C. Sarrazin, E. Bamberg, and J.J. Abbott, "Velocity control with gravity compensation for magnetic helical microswimmers", *Adv. Robotics*, (2011), vol. 25, no. 8, pp. 1007-1028.

7. T. Xu, G. Hwang, N. Andreff, and S. Régnier, "Planar path following of 3-D steering scaled-up helical microswimmers", *IEEE Trans. Robot.*, Feb. 2015, vol. 31, no. 1, pp. 117-127.

8. I.S.M. Khalil *et al.*, "Near-surface effects on the controlled motion of magnetotactic bacteria", In: *Proc.* , *IEEE ICRA*, Jul. 2017, pp. 5976–5982.

9. H.O. Caldag and S. Yesilyurt, "Trajectories of magnetically-actuated helical swimmers in cylindrical channels at low Reynolds numbers", *J. Fluid Struct.*, Okt. 2019, vol. 90, pp. 164-176.

10. L. Li and S.E. Spagnolie, "Swimming and pumping of rigid helical bodies in viscous fluids", *Phys. Fluids*, Apr. 2014, vol. 26, no. 4.

11. Islam S.M. Khalil *et al.*, "Robust and Optimal Control of Magnetic Microparticles inside Fluidic Channels with Time-Varying Flow Rates", *Int. J. Adv. Robot. Syst.*, Jun. 2016, vol. 13, no. 3.

12. B.J. Nelson, I.K. Kaliakatsos, and J.J. Abbott, "Microrobots for Minimally Invasive Medicine", *Ann. Rev. of Biomed. Eng.*, Jul. 2010, vol. 12, no. 1, pp. 55-85.

13. I.S.M. Khalil *et al.*, "Mechanical Rubbing of Blood Clots Using Helical Robots under Ultrasound Guidance", *IEEE Robot. Autom. Lett.*, Apr. 2018, vol. 3, no. 2, pp. 1112-1119.

14. S. Martel *et al.*, "Automatic navigation of an untethered device in the artery of a living animal using a conventional clinical magnetic resonance imaging system", *App. Phys. Lett.*, Feb. 2007, vol. 90, no. 11.

15. P.B. Nguyen *et al.*, "Real-time microrobot posture recognition via biplane X-ray imaging system for external electromagnetic actuation", *IJCARS*, Nov. 2018, vol. 13, no. 11, pp. 1843-1852.

16. J. Gray and G.J. Hancock, "The Propulsion of Sea-Urchin Spermatozoa", *J. Exp. Biol.*, (1955), vol. 32, no. 4, pp. 802-814.

17. R. Cortez, "The method of regularized stokeslets", *SIAM J. Sci. Stat. Comput.*, (2002), vol. 23, no. 4, pp. 1204-1225.

18. J.J. Abbott, E. Diller, and A.J. Petruska, "Magnetic Methods in Robotics", *Ann. Rev. of Control, Robot., Auton. Sys.*, May. 2020, vol. 3, no. 1, pp. 1-3.

19. I.S.M. Khalil, A.F. Tabak, K. Sadek, D. Mahdy, N. Hamdi, and M. Sitti, "Rubbing Against Blood Clots Using Helical Robots: Modeling and in Vitro Experimental Validation", *IEEE Robot. Automat. Lett.*, Apr. 2017, vol. 2, no. 2, pp. 927-934.

20. A.T. Chwang and T.Y.T. Wu, "Hydromechanics of low-Reynolds-number flow. Part 2. Singularity method for Stokes flows", *J. Fluid Mech.*, Feb. 1975, vol. 67, no. 4, pp. 787-815.

21. R. Cortez, L. Fauci, and A. Medovikov, "The method of regularized Stokeslets in three dimensions: Analysis, validation, and application to helical swimming", *Phys. Fluids*, Mar. 2005, vol. 17, no. 3.

22. Bruce, "Helical Swimming Simulator." mathwork.com. https://nl.mathworks.com/matlabcentral/fileexchange/39265-helical-swimming-simulator (accessed May. 6, 2020).

23. C. Brennen and H. Winet, "Fluid Mechanics of Propulsion by Cilia and Flagella", *Ann. Rev. Fluid Mech.*, Jan. 1977, vol. 9, no. 1, pp. 339-398.

24. A.P. Aguiar, D.B. Dačić, J.P. Hespanha, and P. Kokotović, "Path-following or reference tracking?", *IFAC Proc. Vol.*, Jul. 2004, vol. 37, no. 8, pp. 167-172.

25. C. Samson, "Mobile robot control Part 2 : control of chained systems and application to path following and time-varying point-stabilization of wheeled vehicles", *INRIA*, (1994).

26. A. Oulmas, N. Andreff, and S. Régnier, "Chained formulation of 3D path following for nonholonomic autonomous robots in a Serret-Frenet frame", In: *Proc.* , *Am Control Conf*, Boston, Jul. 2016. pp. 7275–7280.

27. A. Oulmas, N. Andreff, and S. Régnier, "3D closed-loop swimming at low Reynolds numbers", *Int. J Robot. Res.*, Sept. 2018, vol. 37, no. 11, pp. 1359-1375.